

Ionospheric erosion by Alfvén waves

C. C. Chaston,¹ V. Genot,² J. W. Bonnell,¹ C. W. Carlson,¹ J. P. McFadden,¹ R. E. Ergun,³
R. J. Strangeway,⁴ E. J. Lund,⁵ and K. J. Hwang⁶

Received 17 August 2005; revised 20 October 2005; accepted 25 November 2005; published 7 March 2006.

[1] Using observations from the FAST small explorer spacecraft, we present fields and plasma observations above the dayside auroral oval showing the erosion of ionospheric plasmas from the topside ionosphere by the action of Alfvén waves. Using interferometric techniques, the waves are shown to approximately obey the expected dispersion for Alfvén waves with transverse scales extending from greater than electron inertial lengths down to ion gyroradii. Measurements of the plasma density where these waves are observed show that over latitudinal widths exceeding 100 km total depletion of the cold ionospheric plasma can occur. These depleted regions or cavities are populated by magnetosheath plasmas, upgoing transversely accelerated ionospheric ions, and downgoing field-aligned electrons. The ionospheric ions and field-aligned electrons are distributed as conics and beams, respectively. Poynting flux observations on the density gradients comprising the cavity walls show that these waves are directed downward and focused inward toward regions of lower density. Wave phase velocity measurements, while subject to significant uncertainty, show that the wave vector is directed transversely outward from the cavity. These observations suggest a feedback model for Alfvén wave focusing and ion heating on density gradients that can lead to intense ion outflow from the ionosphere and subsequent depletion of ionospheric plasmas.

Citation: Chaston, C. C., V. Genot, J. W. Bonnell, C. W. Carlson, J. P. McFadden, R. E. Ergun, R. J. Strangeway, E. J. Lund, and K. J. Hwang (2006), Ionospheric erosion by Alfvén waves, *J. Geophys. Res.*, *111*, A03206, doi:10.1029/2005JA011367.

1. Introduction

[2] Low-altitude polar orbiting satellites commonly observe low-frequency electromagnetic fluctuations above the auroral oval [Louarn *et al.*, 1994; Stasiewicz *et al.*, 2000a]. Several studies have shown that these fluctuations are oblique Alfvén waves with perpendicular structuring extending over a range of scales including the electron inertial length and in some cases the ion gyroradii [Wahlund *et al.*, 1998; Stasiewicz *et al.*, 2000b; Chaston *et al.*, 2004]. The plasma environment in which these waves are observed is usually characterized at altitudes below 1 Earth radii by plasma density gradients, field-aligned accelerated electrons, and transversely accelerated ions [Wahlund *et al.*, 1994; Stasiewicz *et al.*, 1997; Knudsen and Wahlund, 1998; Andersson *et al.*, 2002]. Several studies have shown how a spectrum of dispersive

Alfvén waves can produce the observed field-aligned electron distributions [Kletzing, 1994; Thompson and Lysak, 1996; Chaston *et al.*, 2000; Su *et al.*, 2004] and provide ion acceleration if scales of the order of the ion gyroradii are present [Stasiewicz *et al.*, 2000c; Chaston *et al.*, 2004]. However, there has been comparatively little attention given to the importance of strongly localized transverse plasma density gradients above the auroral oval on Alfvén wave propagation with the exception of publications by Seyler *et al.* [1995], Rankin *et al.* [1999], Lu *et al.* [2003], and Genot *et al.* [1999, 2004]. This is a significant omission, since often the most intense fields fluctuations are observed to be localized in field-aligned density cavities [Stasiewicz *et al.*, 1998] and dispersive Alfvén waves have been found localized in field-aligned density striations in laboratory plasmas [Maggs and Morales, 1996].

[3] At altitudes as low as ~ 1000 km it has been demonstrated that the cavities in which Alfvén waves are imbedded are depleted, and in some cases devoid, of cold ionospheric plasmas with $d\eta/n \sim 1$ [Chaston *et al.*, 2000]. Since the ionosphere is the dominant source of plasma at altitudes at least below $1 R_E$, there must be some means by which this plasma is transported either vertically or radially to provide the cavitation. There have been a number of studies addressing the formation of density cavities by Alfvén waves in the auroral plasma based on various interpretations of the ponderomotive force associated with these waves. Li and Temerin [1993] showed through test particle simulations how plasma could be extracted from the auroral ionosphere due to the ponderomotive force associ-

¹Space Sciences Laboratory, University of California, Berkeley, Berkeley, California, USA.

²Centre d'Etude Spatiale Rayonnements, Toulouse, France.

³Laboratory for Atmospheric and Space Physics, University of Colorado, Boulder, Colorado, USA.

⁴Institute for Geophysical and Planetary Physics, University of California, Los Angeles, Los Angeles, California, USA.

⁵Space Science Center, University of New Hampshire, Durham, New Hampshire, USA.

⁶Physics and Astronomy, Dartmouth College, Hanover, New Hampshire, USA.

ated with the gradient in altitude of the perpendicular wave electric field amplitude.

[4] *Bellan and Stasiewicz* [1998] suggest that density cavitation in Alfvén waves may occur through a parallel ponderomotive force associated with the oscillating field-aligned current in the wave. However, a comparison of cavity depth with the predicted depth for observed field-aligned current amplitudes indicated that this model was unable to yield sufficiently deep cavities [*Chaston et al.*, 2000]. *Shukla and Stenflo* [1999] suggested that the parallel ponderomotive force balancing the thermal force due to Joule heating in the Alfvén wave field in the ionosphere may be sufficient to account from the depletions observed. This was supported by observations of the cavity depth and calculation of the Joule heating expected for observed wave amplitudes. However, given the almost collisionless nature of plasmas in the upper reaches of the ionosphere where these cavities are often observed, the efficacy of this mechanism at altitudes above ~ 1000 km altitude is questionable.

[5] From nonlinear fluid simulations, *Rankin et al.* [1999] have suggested that density perturbations due to the ponderomotive force associated with the nonlinear saturation of field line resonances (FLRs) above the aurora may be the source of density cavities observed. These density perturbations take the form of a driven ion acoustic wave or slow mode Alfvén wave in the presence of perpendicular gradients in the plasma pressure. This work gives a more complete representation of the effects modeled from the single particle cold plasma perspective by *Li and Temerin* [1993] to show that the plasma is “accelerated locally” all along the field line by parallel gradients in the shear wave pressure. In a related study by *Lu et al.* [2003] the assumptions of weak nonlinearity implicit in the work of *Rankin et al.* [1999] were removed. It was demonstrated in this work that FLRs become latitudinally localized inside density cavities due to dispersion and nonlinear effects. This process has been demonstrated to produce density depletions of sufficient depth and width to account for observations from FAST and other auroral satellites; however, the timescale for cavity formation is of the order of an FLR wave period (~ 8 min or more above the aurora).

[6] The observations presented in this report (specifically those showing transverse ion acceleration); however, suggest a mechanism for the formation of Alfvénic density cavities above the auroral ionosphere not necessarily dependent on the ponderomotive force but similar to those processes thought to responsible for the formation of what have become known as “lower hybrid cavities” [*Shuck et al.*, 2003]. In the proposed mechanism an incoming Alfvén wave becomes focused into shallow density dips in the topside ionosphere in a manner similar to that proposed by *Rankin et al.* [2005]. Wave refraction and

phase mixing on the transverse density gradient produce transverse structuring of the wave field in these dips leading to ion and electron acceleration and plasma outflow from the dip to form a cavity. As this process proceeds the density gradients comprising the cavity walls become ever steeper as the plasma is evacuated leading to more rapid phase mixing and more rapid outflow and hence more rapid plasma depletion from the cavity which gets wider. Eventually, multiple cavities may merge to provide wide regions of plasma depletion or eroded ionosphere as observed.

[7] We begin in section 2 by presenting an overview of observations from the FAST satellite from a traversal above the dayside auroral oval where ionospheric density cavitation and electromagnetic waves are observed. In section 3 we employ interferometric techniques to identify these electromagnetic fluctuations as dispersive Alfvén wave turbulence extending over scales including the electron inertial length λ_e and the energetic oxygen gyroradii ρ_{O+} . Then in section 4 we explore the plasma processes occurring within an Alfvénic density cavity in more detail. Specifically, measurements of the wave Poynting flux and interferometric techniques are used to demonstrate that the incoming Alfvén waves from the magnetosphere become focused on the cavity and are refracted by the cavity walls to produce perpendicular field structures on small transverse scales. In section 5 we present a schematic model based on the observations and compare the observations to PIC and fluid simulation results and observations made of lower hybrid density cavities before concluding with a brief summary of the most important observational results.

2. Observations of Plasma Cavitation and Electromagnetic Waves

[8] Figure 1 shows observations from the FAST satellite as it passed through a region of magnetosheath precipitation above the dayside auroral oval at an altitude of ~ 1700 km before entering the polar cap. The magnetosheath ion population can be seen in the first panel at energies above ~ 200 eV. At energies below 100 eV a second ion population can be identified. The mass spectrometer data shows that these ions are primarily O^+ , suggesting that they are of ionospheric origin. Figure 1b shows that these ionospheric ions are observed transverse to the geomagnetic field at pitch angles slightly larger than 270 degrees, showing that they have been locally accelerated perpendicular to B_0 . Integration of these data, as shown in Figure 1c, indicates that these ions are outflowing from the ionosphere at a rate of up to 10^9 ions cm^{-2}/s . A simple calculation shows that without replenishment the observed rate of ion outflow would lead to total depletion of the ionosphere on these fieldlines in ~ 60 min.

Figure 1. FAST observations of dayside ionospheric erosion. (a) Ion energy spectrogram for the hemisphere opposite to the spacecraft velocity vector. (b) Ion pitch angle spectrogram covering the hemisphere opposite to the spacecraft velocity vector. (c) Integrated field-aligned ion flux over the same pitch angle range. (d) Electron energy spectrogram. (e) Electron pitch angle spectrogram. (f) Electric field measured perpendicular to B_0 along the spacecraft trajectory and pointing roughly northward. (g) Power spectra of the electric field data shown in Figure 1f. (h) Magnetometer measurements perpendicular to B_0 and pointing roughly eastward; black is the fluxgate measurement alone and red is fluxgate plus search coil measurement. (i) Langmuir probe current (black) and field-aligned current from the electrostatic analyzer experiment on FAST (see text for explanation).

[9] Similar plasma sources can account for the observed electron populations. Precipitating magnetosheath electrons can be identified in Figure 1d by the peak in energy flux observed at ~ 200 eV. Partly obscuring this peak, particu-

larly after 0644:47 UT, we can identify suprathermal electron bursts [Johnstone and Winningham, 1982]. Figure 1e shows that these bursts are largely field-aligned and down-going (180°). Since the differential energy fluxes of these

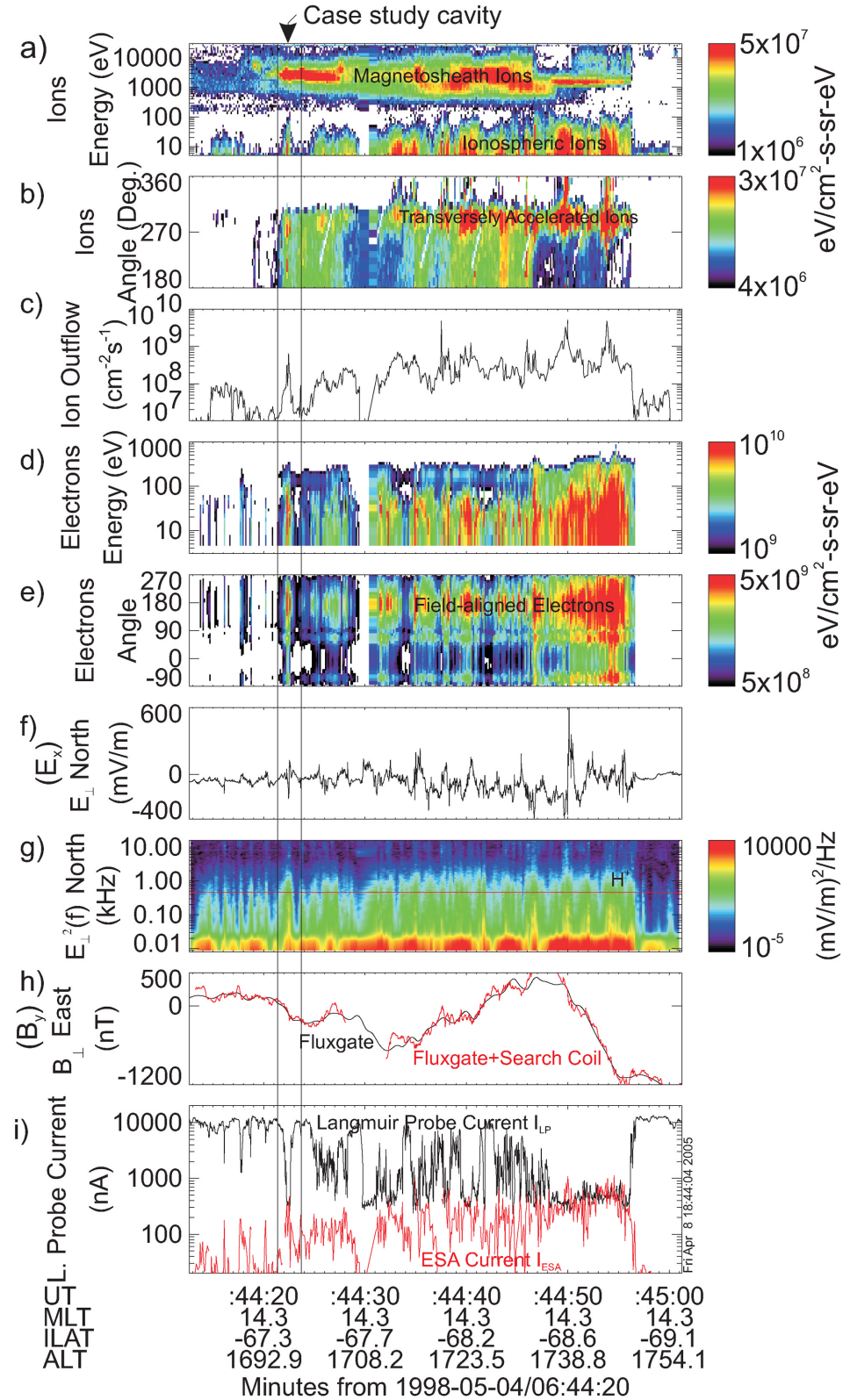


Figure 1

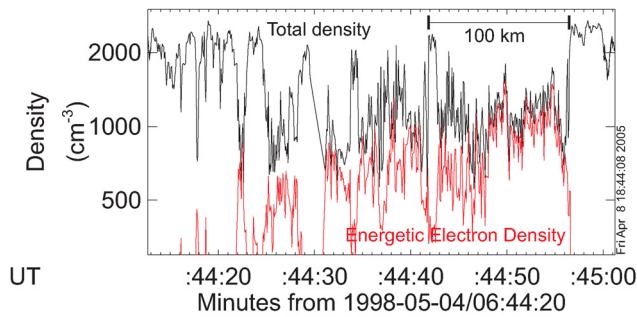


Figure 2. Calibrated Langmuir probe data (black) from Figure 1i and electron density from the electrostatic analyzer experiment. The calibration method is described in the text.

bursts decrease (albeit slowly) with energy from the lowest measured (5eV), it is speculated that they are predominately ionospheric electrons which have been accelerated along B_0 .

[10] These enhanced ion and electron fluxes are observed coincident with fluctuations in the electric and magnetic field measurements. Figure 1f shows the electric field measured in the spacecraft spin plane, perpendicular to the geomagnetic field, and pointing roughly northward along the spacecraft trajectory (E_\perp north or E_x). The observed field deviations are impulsive and disordered with no clear periodicity or scaling. Indeed Figure 1g shows that over this interval the wave power falls monotonically with increasing frequency from 0 up to the 16 kHz Nyquist with no structuring in the vicinity of the proton or oxygen gyrofrequencies. A similarly featureless spectrum can be found in the spectra of the magnetic field time series (B_\perp east or B_y) shown in Figure 1h. These data are measured perpendicular to the geomagnetic field and in the eastward direction orthogonal to E_x . This measurement has been performed using both fluxgate and search coil magnetometers, shown here by the black trace representing measurements from the fluxgate magnetometer alone and red traces showing a composite magnetic field measurement from both the fluxgate and search coil magnetometers. For the operating mode of the spacecraft at this time the response of the fluxgate magnetometer falls off steeply above ~ 0.5 Hz above which the search coil magnetometer provides more reliable amplitude measurements. For this reason we have superimposed the search coil measurements on the fluxgate measurement to provide a more continuous representation of fluctuations in B_\perp with increasing frequency.

[11] Typically, electromagnetic fluctuations at low frequencies in space plasmas, such as those shown in Figures 1f–1h, are identified by the ratio of the observed transverse electric (E_x) and magnetic fields (B_y). For field-aligned currents which close through Pedersen currents in the ionosphere this ratio is $E_x/B_y = 1/(\mu_0 \Sigma_p)$, where Σ_p is the height integrated Pedersen conductivity [Sugiura, 1984]. In the spacecraft frame these appear through Ampere's law as temporal variations in B_x due to spacecraft Doppler shift. However Alfvén waves with a finite perpendicular scale or wave number (k_x) also carry field-aligned currents. These field-aligned currents however close locally via polarization drifts and provide an imped-

ance ratio given by $E_x/B_y = V_A(1 + k_x^2 \lambda_e^2)^{1/2}$ [Goertz and Boswell, 1979] where $\lambda_e = c/\omega_p$ is the electron inertial length and ω_p is the electron plasma frequency. For the data shown in Figures 1f–1h E_x/B_y is spacecraft frame frequency dependent. For variations in B_x and E_y averaged over windows of width greater than 5s (~ 50 km in the ionosphere) $E_x/B_y \approx 1/(\mu_0 \Sigma_p)$ for $\Sigma_p = 1-10$. However, at frequencies above 1 Hz in the spacecraft frame this ratio becomes more like V_A and at higher frequencies becomes increasingly electrostatic. Since V_A and λ_e are density dependent, to identify these electromagnetic fluctuations as Alfvén waves based on the observed E_x/B_y ratio requires a measurement of the density and also of k_x . These measurements are nontrivial and constitute the majority of the analysis performed in this manuscript. We now discuss how we obtain reliable density measurements for the interval shown in Figure 1 and then in section 3 demonstrate that the density profile is highly fractured due to the action of dispersive Alfvén waves identified using interferometric measurements.

[12] The observed field fluctuations are colocated with rapid variations in the current measured by the Langmuir probe (I_{LP}) and shown in Figure 1i by the black trace. The red trace in this panel is the current to the Langmuir probe from the field aligned motion of electrons as measured by the electrostatic analyzer experiment (I_{ESA}). This current has been evaluated by subtracting fluxes from the ESA measurements at energies below the spacecraft potential (which can be up to 20 V positive at this time), calculating the required moments and multiplying by the cross-sectional area of the Langmuir probe. From Figure 1i it can be seen that I_{ESA} forms a lower bound for I_{LP} . This leads us to write $I_{LP} = I_{thermal} + I_{ESA}$ where $I_{thermal}$ is the contribution to I_{LP} from the thermal plasma current. When $I_{LP} = I_{ESA}$ the dominant current to the probe is that due to field-aligned electrons. Since the Langmuir probe is biased 15 V positive with respect to the satellite this indicates that at these times the total current is carried by electrons with energies of at least 15 eV. Consequently, it can be concluded that when $I_{LP} = I_{ESA}$ the measured plasma at these times is devoid of the usually dominant ambient ionospheric component (which usually provides the thermal plasma current to the LP) and the total plasma density is given by the moment of the ESA observations taken at energies above the spacecraft potential.

[13] Outside those regions where I_{LP} is depressed we observe plasma emissions allowing us to calibrate I_{LP} to give the density of the thermal plasma. This has been determined statistically using this event and other similar events at approximately the same altitude to be $n_{thermal} \sim (0.2 \pm 0.1) I_{thermal}$ for sphere 6 on FAST when operated in current mode (under the assumption that the cold ionospheric or thermal plasma temperature is roughly the same throughout). To obtain density measurements where the current to the probe is a mixture of the thermal current due to the ambient ionospheric plasma and that due to field-aligned electrons, the density is given by subtracting I_{ESA} from the I_{LP} to give $I_{thermal}$ and then using the above calibration to give the thermal plasma density. The total density is then given by adding the thermal plasma density to that measured by the ESA above the spacecraft potential. The net result for total density in this case is shown in

Figure 2. This result shows sections over horizontal widths of >100 of km (based on a spacecraft speed of ~ 7 km/s) where the cold or thermal ionospheric plasma has been completely removed and replaced by significantly smaller densities of energetic electrons (red) (which are field-aligned). Significantly, it is in those regions where the cold ionospheric plasma has been depleted that the largest oscillations in the field quantities are observed.

3. Cross Spectral Measurements and Alfvénic Turbulence

[14] With a reliable measurement of density in hand, we now require a measurement of the wavevector to identify the electromagnetic fluctuations based on E_x/B_y . To achieve this, we employ interferometric techniques to determine an average value for \mathbf{k} in the spin plane (\mathbf{k}_{sp}). This approach is similar to that exploited by *Wahlund et al.* [1998] and *Stasiewicz et al.* [2000b] using Freja measurements with the exception that we employ a wavelet based approach and obtain a two-dimensional (2-D) measurement of the wavevector. In this approach the wave vector is determined by measuring the phase difference between electric field measurements in the spin plane at multiple points separated by a known distance in this plane [Labelle and Kintner, 1989]. The FAST satellite provides several such baselines allowing interferometric measurements such as these to be performed. This technique as applied to observations from the FAST spacecraft is described in Appendix A.

[15] The results from the interferometric analysis using equation (A1) from Appendix A are shown in Figure 3. These results represent an average taken over the entire interval contained in Figure 1. In obtaining these results, we have excluded those measurements with two-point coherency less than 0.7 and those intervals where either one of the baseline are within 10° of the projection of the geomagnetic field into the spin plane. We have also excluded those transforms with rapidly or erratically varying phase with frequency. These exclusions significantly reduce the temporal resolution of the measurements made but provide a more reliable average result. The error bars shown throughout Figure 3 represent one standard deviation in the averaged results. These are of course symmetric about the averaged value but with some exceptions are generally plotted in one direction only due to the logarithmic scaling.

[16] Figure 3a shows the variation of k_{sp} with spacecraft frame frequency. The red line shows the expected result for field structures which are stationary in the plasma frame and provide the observed spacecraft frame frequency purely through spacecraft Doppler shift. Up to about 200 Hz the Doppler-shift yields a reasonable approximation of the wave numbers and is well within one standard deviation of the averaged value as shown by the error bars. Figure 3b shows the angle between \mathbf{k}_{sp} and the projection of the geomagnetic field (\mathbf{B}_o) into the spin plane (\mathbf{B}_{sp}). For the interval considered \mathbf{B}_o and \mathbf{B}_{sp} are separated by $\sim 5^\circ$. Over the frequency range plotted we find angles ranging between 80° and 85° . These angles represent a lower limit of the actual angle between \mathbf{k} and \mathbf{B}_o since it is probable that an unmeasured component of \mathbf{k} exists perpendicular to the spacecraft spin plane. Owing to the inclination of the spin plane relative to \mathbf{B}_o , the presence of this unmeasured

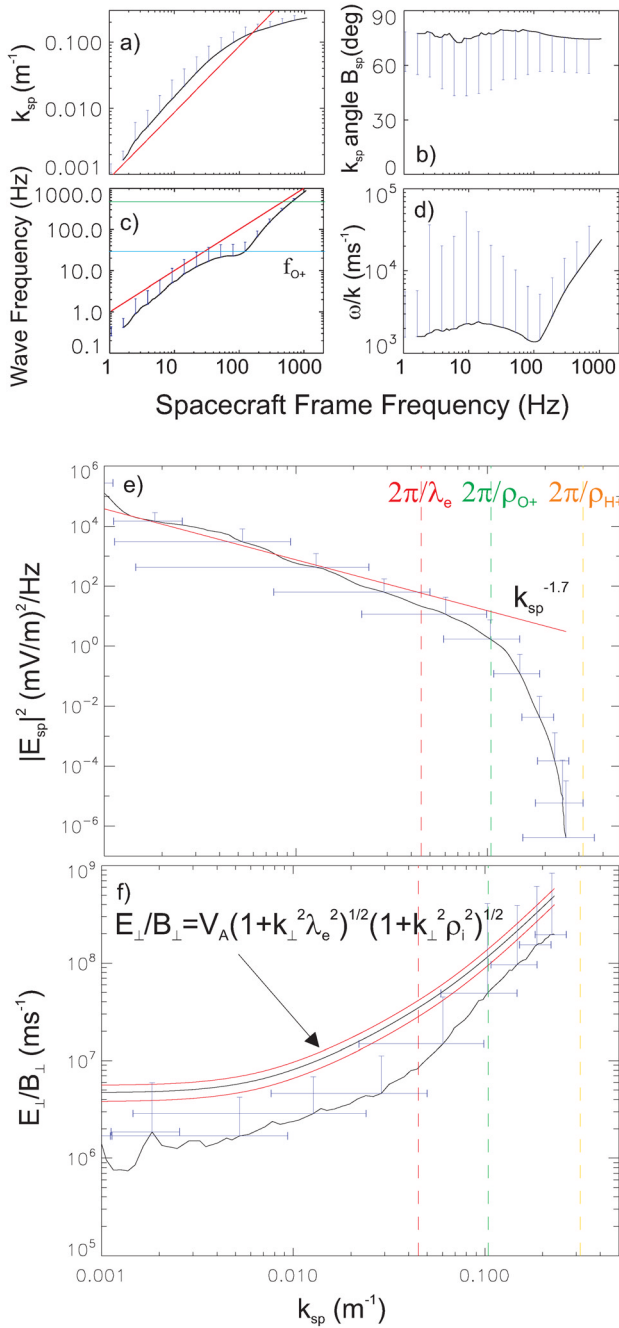
component means that the magnitude of \mathbf{k} along \mathbf{B}_{sp} will be over estimated and hence the angle of \mathbf{k} to \mathbf{B}_o under-estimated. Nonetheless, in the measurements presented in this panel it should be noted that the averaged values are everywhere within one standard deviation of being exactly perpendicular and so $\theta_{sp} \rightarrow 0^\circ$ (where θ_{sp} is the angle between the spacecraft velocity vector and \mathbf{k} in the satellite spin plane).

[17] Figure 3c shows the wave frequency in the plasma frame. This has been obtained by subtracting the spacecraft Doppler shift from the observed spacecraft frame wave frequency. In performing this calculation we have included the contribution from the poleward plasma convection of ~ 1 km s $^{-1}$ estimated by integrating the measurements from the ion spectrometer experiment. Since the Doppler shift and the spacecraft frame frequency over most of the observed frequency range have very similar magnitudes the errors in the wave frequency are large. Because of this the averaged wave frequencies shown here represent an upper limit for ω_{sp} with the magnitude of the error bars indicating that within 1 standard deviation of the average values we find a wave frequency of 0 Hz. The blue and green horizontal lines in this panel show the value of the local oxygen (f_{O+}) and hydrogen cyclotron frequencies (f_{H+}), respectively. From these observations it can confidently be said that ω_{sp} in the plasma frame is less than Ω_{O+} for spacecraft frame frequencies at least below 100 Hz in the spacecraft frame. Figure 3d shows the wave phase speed ω_{sp}/k_{sp} . As with the wave frequency measurement the errors in evaluating this quantity are substantial. However, a time domain cross-correlation analysis to be discussed in the next section also yields phase speeds similar to these values.

[18] The identification of the field fluctuations as turbulence requires scale invariance in the observed wave power spectra. Figure 3e shows the k-spectra of the observations in the spin plane. The red line represents a $k_{sp}^{-1.7}$ the power law spectra fitted to the observations over the first decade on the k-scale. This is the expected dependency for Komolgorov fluid turbulence. Beyond this range the wave power falls ever more rapidly with increasing k_{sp} . The red dashed vertical line in this plot shows the wave number corresponding to the electron inertial length (i.e., where $k_{sp} = 2\pi/\lambda_e = 2\pi/145$ m $^{-1}$). Clearly, there are scales present in the observed field fluctuations that extend downward to include this length. Interestingly, it is at wave numbers a few times smaller than $2\pi/\lambda_e$ that the observed k-spectra begins to deviate from the Komolgorov like power-law. In the local approximation, and for the parameters present at this altitude, the wave dispersion for an electromagnetic wave at frequencies below Ω_{O+} and at small transverse scales can be described by $\omega/k_{\parallel} = V_A(1 + k_{\perp}^2 \lambda_e^2)^{-1/2}$ [Goertz and Boswell, 1979]. This wave carries a parallel electric field given by $E_{\parallel}/E_{\perp} = k_{\perp} k_{\parallel} \lambda_e^2 / (1 + k_{\perp}^2 \lambda_e^2)$. Consequently, when $k_{\perp} \lambda_e \rightarrow 1$ the wave becomes dispersive and may dissipate through electron Landau damping to provide the observed deviation from the power law spectra for $k_{\perp} \lambda_e \geq 1$.

[19] The other dashed vertical lines in this panel represent wave numbers given by the inverse oxygen and hydrogen gyroradii (i.e., where $k_{sp} = 2\pi/\rho_{O+} = 2\pi/60$, shown by the green line, and $k_{sp} = 2\pi/\rho_{H+} = 2\pi/20$, shown by the orange line) of the energetic ionospheric plasma. These are measured by the FAST mass spectrometer calculated over the

energy range from 5 to 100 eV for the backward looking hemisphere of the instrument to avoid the influence of magnetosheath ions and the effects of spacecraft ram, respectively. The energies from this measurement averaged over the interval shown in Figure 1 are ~ 10 eV and 18 eV, respectively. These energies do not represent the temperature of the bulk ionosphere but rather the average energy of the tail of the ionospheric distribution at energies above 5 eV. It is shown in Figure 2a that the density of this energetic portion of the ion distribution can be as large as few 100 cm^{-3} within regions of depleted density. The observed wave numbers shown indicate wave scales extending down to and including the energetic oxygen gyroradius but with wave power falling sharply at smaller scales and failing to reach the energetic proton gyroradius.



It has been shown previously that at wave scales approaching ion gyroradii electromagnetic waves in this frequency range may strongly energize ions and thereby dissipate [Chen et al., 2001]. Dissipation by this means may account for the increasing rate of decline in $E_{\text{sp}}^2(k_{\text{sp}})$ for $k_{\perp\rho_{O+}} \geq 1$. These observations are consistent with that expected for turbulence with power-law like k -spectra containing inertial and dissipation subranges.

[20] To establish that we are observing specifically Alfvénic turbulence, we compare the wave impedance with the expected dispersion for small-scale Alfvén waves in the observed plasma environment. It is well known in the local approximation that this is given by

$$\frac{E_x}{B_y} = V_A \sqrt{(1 + k_x^2 \lambda_e^2)(1 + k_x^2 \rho_i^2)(1 - \omega^2 / \Omega_i^2)}, \quad (1)$$

where ρ_i is the average ion gyroradius and ω is the wave frequency in the plasma frame. For wave frequencies in the plasma frame approaching Ω_i , this relation provides essentially electrostatic waves and is invalid for waves where $\omega \geq \Omega_i$. In calculating the predicted E_x/B_y ratio from this expression we ignore the finite frequency correction. This is because the errors given by the standard deviation in the measured wave frequency are significantly larger than the average wave frequency and extend to include 0 Hz. This does alter significantly the result below frequencies of 100 Hz in the spacecraft frame (or $k_{\text{sp}} \leq 0.1$). Figure 3f shows the comparison between the observed E_x/B_y ratio and the predicted ratio from equation (1) as functions of k_{sp} . Each red line represents the predicted result but with V_A shifted by one standard deviation above and below its average value. The error bars on the observed E_x/B_y curve show that the model prediction lies with one standard deviation of the observations throughout, but generally predicts a wave somewhat more electrostatic than is observed. Given the highly variable density profile throughout this interval this is not an unexpected result since it has been shown elsewhere that coupling to drift modes on density gradients can provide smaller E_x/B_y ratios than found in the homogeneous case [Chaston et al., 2005] given by equation (1). In addition these waves may have wavelengths along the B_o sufficiently large that the variation in the Alfvén speed along the field over one

Figure 3. Wave properties from interferometry. (a) Wave number in the spin plane (k_{sp}). (b) Angle between k_{sp} and B_o in the spin plane. (c) Wave frequency; the blue line is the oxygen gyrofrequency (f_{O+}), and the green line is the proton gyrofrequency (f_{H+}). (d) Wave phase speed in the spin plane. (e) Power spectra of the wave electric field in the spin plane as a function of k_{sp} . The vertical red line represents $k_{\text{sp}} = 2\pi/\lambda_e$ where λ_e is the average electron inertial length, the green line represents $k_{\text{sp}} = 2\pi/\rho_{O+}$ where ρ_{O+} is the average oxygen gyroradius, and the orange line represents $k_{\text{sp}} = 2\pi/\rho_{H+}$ where ρ_{H+} is the average proton gyroradius. The sloping red line is a fit of a $k^{-1.7}$ spectral law to the first decade of observations in k_{sp} . (f) Ratio of perpendicular to B_o electric field (E_x or E_{\perp}) in the spin plane to the magnetic field (B_y or B_{\perp}) perpendicular to both B_o and the spin plane. The black line shows the expected result for inertial Alfvén waves with the red lines showing one standard deviation in V_A . The error bars throughout show 1 standard deviation from the average.

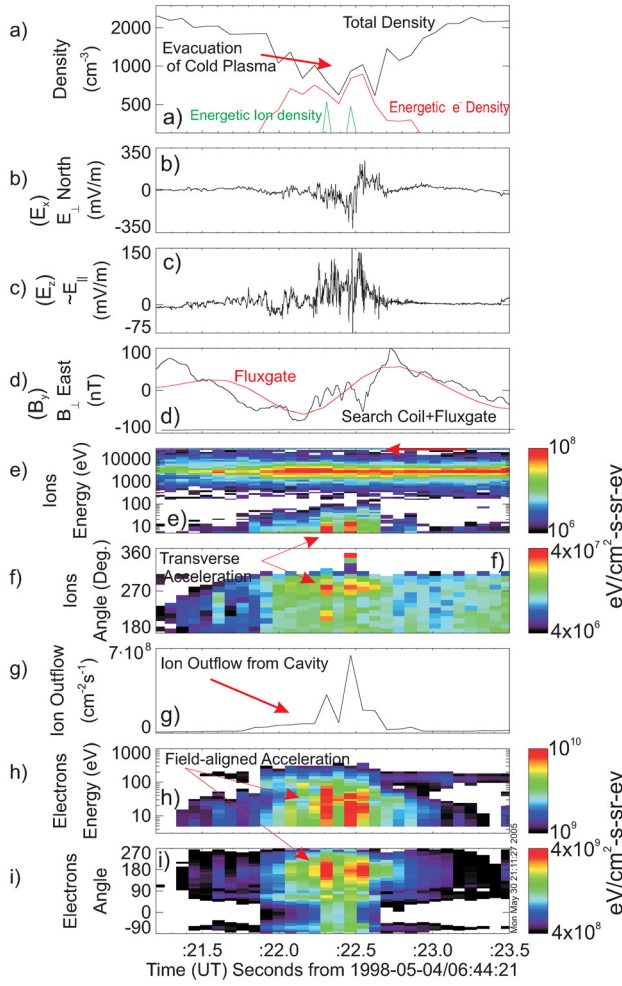


Figure 4. Individual cavity case study. (a) Density from the calibrated Langmuir probe (black), electrostatic analyzer for electrons (red), and electrostatic analyzer for ions (green). (b) Perpendicular to B_0 electric field pointing roughly northward (E_x or E_{\perp}). (c) Approximate parallel to B_0 electric field (E_{\parallel} or E_z). (d) Magnetic field measurements perpendicular to B_0 and pointing roughly eastward (B_y or B_{\perp}). The red trace is from the fluxgate magnetometer and the black trace from the fluxgate magnetometer plus the search coil magnetometer. (e) Ion energy spectrogram for the hemisphere opposite to the spacecraft velocity vector. (f) Ion pitch angle spectrogram for the hemisphere opposite to the spacecraft velocity vector. (g) Integrated ion flux for the hemisphere opposite to the spacecraft velocity vector. (h) Electron energy spectrogram. (i) Electron pitch angle spectrogram.

wavelength may be significant. In this case a nonlocal analysis is required including the effects of ionospheric reflection as performed by Lysak [1998]. For the lowest-frequency shear Alfvén waves identified in this study the local analysis suggests a parallel wavelength of at least 1000 km; almost the distance from the satellite to the ionosphere. At higher frequencies these wavelengths will be smaller and more consistent with the use of a local approximation. However, since the trend observed in E_x/B_y matches the predicted results to within one standard

deviation, we identify these waves as dispersive Alfvén waves.

4. Inside an Alfvénic Density Cavity

[21] To identify the processes occurring within these density depletions, we now examine the fields and plasma within a single “well behaved” cavity as shown in Figure 4 and identified in Figure 1. Figure 4 a shows a Gaussian-shaped depression created by the depletion of the cold thermal ionospheric plasma. This is indicated by the close agreement between the total density and the energetic electron density. Figures 4b, 4c, and 4d show that localized within the transverse width of the cavity are electromagnetic fluctuations. The large-scale electric field structure underlying the oscillations shown in Figure 4b indicates an electric field pointing southward then northward across the cavity. Since the spacecraft at this time is moving southward these fields are converging. In the electrostatic interpretation [Mozer *et al.*, 1977] this suggests excess negative charge within the cavity and the presence of upward parallel electric fields at this altitude or some altitude below the spacecraft. Figure 4c shows the electric field projected along B_0 in the satellite spin plane. Since the spin plane at this time is within $\sim 5^\circ$ of B_0 this measured field provides an indication of the parallel electric field across the cavity (E_z or E_{\parallel}). (Alternatively, these fields could be explained by transverse electric fields in the direction of the spacecraft spin axis; however, these would need to exceed 1V/m to account for the observations). This field has a significant DC component directed upward across the base of the cavity consistent with the direction of the converging transverse fields in the electrostatic interpretation. Figure 4d shows the magnetic field measured across the cavity from the search coil and fluxgate magnetometers filtered above 0.5 Hz. The black trace in this panel is a composite measurement from the search coil and fluxgate magnetometers while the red trace is the result from the fluxgate magnetometer alone. These measurements show the presence of field-aligned currents on a variety of scales across the width of the cavity.

[22] The enhanced electric and magnetic field fluctuations within the density cavity are colocated with enhanced ion and electron fluxes shown in the remaining panels. The burst of ions at energies below 100 eV shown in Figure 4e has its peak fluxes coincident with the largest electric field amplitudes. The integrated result shown in Figure 4g indicates that these ions provide significant fluxes of upward moving ions from the base of the cavity. Figure 4f shows that these ions are distributed largely at angles just greater than 270° indicating some form of transverse acceleration. In the same panel we can also identify a very brief burst of upgoing ions at angles close to 360° consistent with the existence of the quasi-stationary parallel electric field shown in Figure 4c. The electrons within the cavity as shown in Figures 4h and 4j have energies generally less than 200 eV and are distributed largely along the geomagnetic field and flow downward (180°) toward the Earth. These observations suggest that these cavities are regions where waves become focused, produce small-scale transverse structure, and subsequently cause field-aligned electron acceleration and transverse ion acceleration.

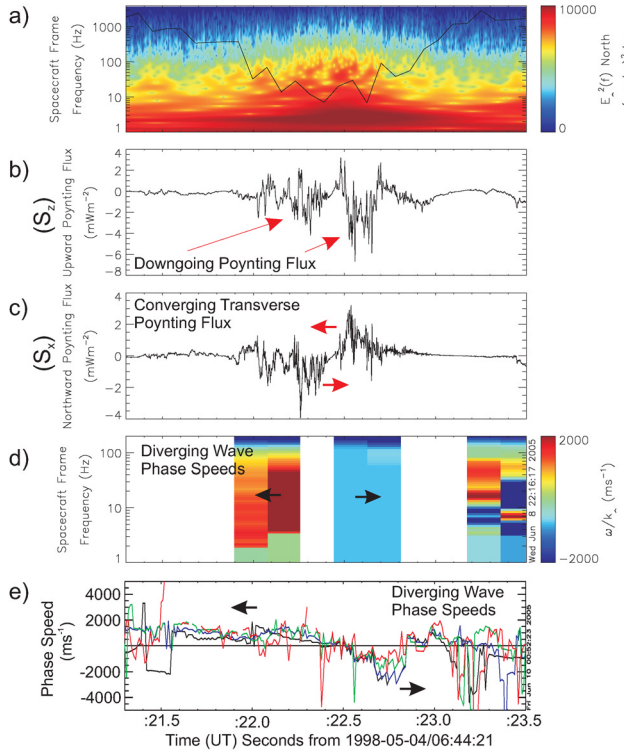


Figure 5. (a) Wavelet spectrogram of the perpendicular to B_0 wave electric field pointing roughly northward (E_x or E_{\perp}), the black trace is scaled density. (b) Field-aligned wave Poynting flux (S_z). (c) Transverse wave Poynting flux (S_x). (d) Wave phase speed spectrogram from interferometry. (e) Wave phase speed from a time domain cross correlation analysis for fluctuations above 2.5 (black), 5 (blue), 10 (green), and 20 Hz (red).

[23] Figure 5 provides evidence for the focusing of incoming wave power into the density depletion. Figure 5a shows the wave power peaking in the density depletion as indeed was found for all the observed density depletions shown in Appendix A as Figure A2. Figure 5b shows the estimated field-aligned wave Poynting flux. This quantity has been calculated using the composite 3-D search coil/fluxgate magnetometer measurements and E_x above 0.5 Hz. Since the fluctuation amplitudes in B_y are significantly larger than in B_x , and the polarization of the electric field in such events from FAST has been shown previously to be aligned north-south [Stasiewicz *et al.*, 2000a], the unmeasured contribution to the field-aligned wave Poynting flux, $|E_y B_x|/\mu_0$, is expected to make a smaller contribution to the field-aligned Poynting flux than $|E_x B_y|/\mu_0$. Consequently, S_z shown here is representative of the field-aligned Poynting flux. Significantly, the largest field-aligned Poynting fluxes are observed on the walls of the cavity with somewhat of a gap in the center of the cavity and are primarily pointing down the magnetic field line toward the Earth. Figure 5c shows that the wave Poynting flux measured along the spacecraft trajectory and perpendicular to B_0 (S_x). Since the field-aligned magnetic wavefield, B_z , is much smaller than the transverse magnetic wavefield the contribution of $|E_y B_z|/\mu_0$ to S_x is minimal unless E_y is larger than 1 V/m. Because fields of this magnitude are rarely measured, it is

reasonable to assume that S_x shown here is a meaningful representation of the northward directed wave Poynting flux. This measurement indicates that the transverse wave Poynting flux is convergent or focused on the cavity with S_x pointing southward and northward on the northern and southern sides of the cavity respectively. Figure 5d shows the wave phase velocity across the cavity in the plasma frame. The gaps here occur where either of the two baselines become close to the projection of B_0 in the spin plane and where the phase variation with ω_{sp} is erratic. As detailed in section 3, this measurement is subject to errors of magnitude similar to the magnitude of the measurements themselves and so are not conclusive. However, the wave phase velocity in the cavity is divergent with v_{sp} pointing northward and southward on the northern and southern sides of the cavity, respectively. This result is confirmed by the time domain result displayed in Figure 5e where the delay between wave phase fronts measured along the x_{58-78} and x_{12-14} baselines has been measured. The colored lines here indicate the transverse wave phase speed for fluctuations above 2.5 (black), 5 (blue), 10 (green), and 20 Hz (red) and indicate divergence from the center of the cavity. The magnitudes of these speeds are similar to those found by the frequency domain technique.

5. Discussion

[24] The observations presented here suggest a model for the propagation of Alfvén waves above the auroral oval and the subsequent acceleration of ionospheric plasmas leading to density cavity formation and the erosion of the auroral ionosphere. A schematic showing Alfvén waves incident on the ionosphere based on these observations is shown in Figure 6. This figure illustrates the refraction of a downward propagating shear Alfvén wave on a preexisting density depression showing specifically the rotation of the phase fronts on the Alfvén speed gradients comprising the cavity

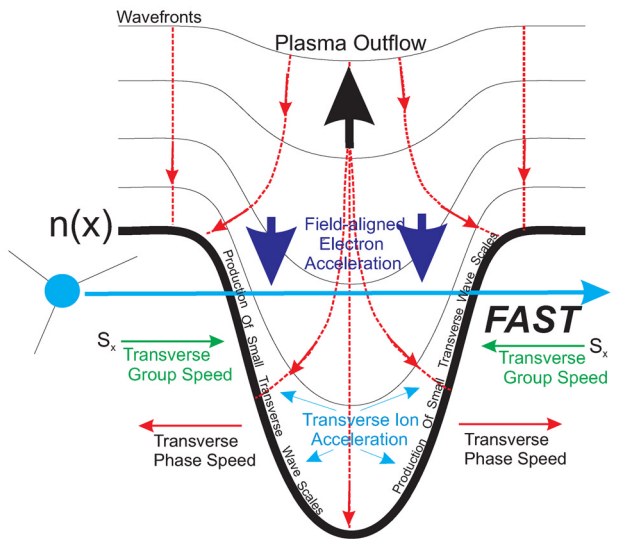


Figure 6. Idealized scheme for the interaction of a shear Alfvén wave with a density cavity above the auroral oval based on observations.

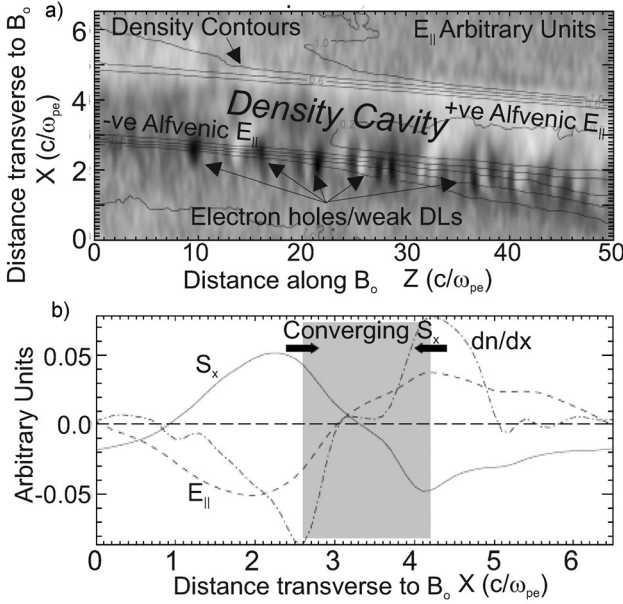


Figure 7. Results from the 2-D PIC simulation of Genot et al. (a) Parallel wavefield (E_{\parallel}) over 1/4 Alfvén wavelengths along the geomagnetic field (Z) and ~ 6 electron skin depths ($\lambda_e = c/\omega_{pe}$) across (X). Gray-scale shows the parallel electric field with positive values shown by lighter shades and negative values by darker shades on a linear scale. Contours show density with a normalized interval of 0.2. (b) Averaged results from Figure 7a. The solid line shows the transverse wave Poynting flux (S_x), the dashed line is E_{\parallel} and the dot-dashed line is the density gradient (dn_0/dx). The gray shaded portion shows the inner cavity bounded by the maxima in the density gradient.

walls. The refraction of the phase fronts on the cavity walls accounts for the outward directed phase velocities found across the cavity as observed in Figure 5. The inward focused Poynting flux observed indicates that the wave group velocity is convergent on the cavity. These observations are consistent with the backward propagating nature of the inertial Alfvén waves where the transverse wave group and phase velocities are oppositely directed [Stasiewicz et al., 2000a]. The observations also suggest that wave refraction on the cavity walls leads to the focusing of Alfvén wave energy within the cavity.

[25] The refraction of the incoming wavefronts on the cavity walls leads to phase mixing and continuously provides smaller scales perpendicular to B_0 at a rate determined by the magnitude of the density gradient. Ultimately, this process is limited by dissipation. As mentioned in section 3 when $\lambda_x \rightarrow \lambda_e$ or ρ_i the wave is damped by field-aligned electron acceleration and transverse ion acceleration, respectively. For the observed parameters phase mixing from the largest scales observed down to scales of the order of λ_e could occur on timescales of the order of seconds (simulations to be discussed later show this time to be less than one Alfvén wave period). Once these scales have been attained and the wave carries an appreciable parallel electric field, instabilities driven by electrons accelerated in these waves may lead to the production of secondary waves with frequencies close to Ω_i causing

transverse ion acceleration/heating via cyclotron resonance or via the disruption of the ion orbit in waves produced by instability on scales approaching ion gyroradii. On the basis of the rather featureless form of the observed wave spectra the second of these acceleration mechanisms seems more probable.

[26] The net result of the production of small-scale structure in k_{sp} is the acceleration and eventual loss of plasma from the cavity. This is facilitated by the mirror force of the diverging geomagnetic field accelerating the transversely accelerated ions upward and ambipolar electric fields acting on ionospheric electrons and dragging them upward with the ions to maintain charge neutrality. The plasma loss from the cavity walls leads to steeper density gradients and hence more rapid phase mixing and stronger focusing. This process leads to larger parallel electric fields and hence stronger electron acceleration and so greater instability. This provides a positive feedback loop, whereby the plasma loss process itself increases the rate of plasma loss. The process may initially be started by the focusing of incoming Alfvén wave Poynting flux due to dispersive effects in preexisting shallow transverse density dips [Rankin et al., 2005]. With several iterations of the feedback loop these dips will deepen to form cavities which will eventually broaden as the density on the cavity edges is depleted. In this way density cavities may be unstable in the presence of Alfvén waves and very deep density cavities may be formed. With sufficient time adjacent cavities may join together to produce the density profile shown in Figure 1 where a large section of the topside auroral ionosphere has been eroded.

[27] The scenario described above has been simulated through the use of fluid codes for linear traveling Alfvén waves by Genot et al. [1999] and in the fully nonlinear case for field line resonances by Lu et al. [2003]. These authors demonstrate the efficacy of transverse density gradients for producing dispersive Alfvén waves on timescales less than an Alfvén wave period. This leads to intensified electric field fluctuations with transverse scales of the order of the electron-inertial length where these gradients exist. Genot et al. [1999] identify an additional contribution to E_{\parallel} in these cavities distinct from the usual E_{\parallel} associated with inertial Alfvén waves in homogeneous plasma due to the polarization drift on these gradients. On density gradients satisfying $(1/n)\partial n/\partial x \geq k_{\perp}$ this contribution can significantly enhance the linear parallel field in the wave leading to enhanced electron acceleration. Alternatively, Lu et al. [2003] show that nonlinear ponderomotive effects steepen the transverse density gradient and thereby accelerate the production of small scales and hence increase the ability of these waves to interact directly with the plasmas populating the cavity. Significantly, the density cavity formation in this case leads to wave trapping within the cavity and the possibility of transverse Alfvén eigenmodes.

[28] Genot et al. [2000, 2001, 2004] have considered the self-consistent kinetic evolution of shear Alfvén waves with density cavity through the use of a 2-D PIC code developed by Mottez et al. [1998]. These authors have been able to follow the initially linear and then nonlinear evolution of the system as a purely parallel ($k_{\perp} = 0$) polarized Alfvén wave encounters a density cavity similar to that presented from

observations in Figure 4a. The results from this simulation are shown in Figure 7 for a 1/4 shear Alfvén wavelength parallel to B_0 (Z). The size of the region simulated corresponds to one full parallel wavelength of the incoming shear Alfvén wave along the geomagnetic field facilitating the use of periodic boundary conditions. While these boundary conditions do not allow an exact comparison with the observations, some salient features emerge. First, as the wave refracts on the density gradients comprising the cavity walls scales of the order of λ_e are formed in $\sim 1/20$ of an Alfvén wave period. The grey-scale in Figure 7a shows a snapshot of E_{\parallel} in the PIC simulation. Large-scale enhancements of E_{\parallel} (lightest and darkest shades) associated with the refraction of the incoming shear wave are found on the transverse density gradients represented by the closely spaced density contours in this panel. This result is most clearly shown, however, by averaging the parallel field of Figure 7a along B_0 to yield the dashed line in Figure 7b which peaks close to the maxima in dn/dx (dot-dashed line in this panel). Second, as shown by the solid line and arrows in Figure 7b, these authors find that the largest Alfvén wave Poynting fluxes are found on the density gradients (dot-dashed lines) and that this Poynting flux is focused inward toward the center of the cavity. This is independent of wave phase and is consistent with the observations from FAST shown in Figure 5c. Third, the field-aligned electron acceleration that occurs in the linear parallel Alfvén wavefield on the density gradient triggers a Buneman instability followed at a later stage by a beam-plasma instability which generates nonlinear electrostatic structures on scales of the order of the Debye length. These structures can be found on the negative transverse density gradient in Figure 7a and are identified as electron holes and weak double layers [Genot et al., 2004]. Typically, these features have electric field amplitudes larger than that of the Alfvén wave field. Such features have been identified in Alfvén waves from FAST when high-resolution field measurements are available. Consequently, these PIC simulations concur with observations to show that the interaction of the Alfvén wave with a density gradient self-consistently produces structuring in the electric field on transverse scales of the order of the cavity itself (several λ_e) down to Debye lengths.

[29] A clear indication of the importance of nonlinear effects in the wave dynamics inside the density cavity is the large magnitude of the parallel electric field observed as shown in Figure 4c which at times exceeds 100 mV/m. This amplitude is more than 2 orders of magnitude larger than given by the linear expression for the parallel electric field due to electron inertia presented in section 3. Observations of this kind in Alfvén waves are however not unusual and have been reported elsewhere by Chust et al. [1998], Stasiewicz et al. [1998], Chaston et al. [1999], and Ergun et al. [2005]; however, the origin of these large fields remains unknown. In the fluid description of the plasma the parallel electric field associated with a field-aligned current, such as that carried by an Alfvén wave, is given by the electron parallel equation of motion [Lysak and Dum, 1983]. This equation shows that the parallel field can be supported by a number of effects including linear [Goertz and Boswell, 1979], nonlinear [Ronmarck, 1999] electron inertia, parallel electron pres-

sure gradients [Hasegawa, 1976], and anomalous resistivity [Lysak and Carlson, 1981; Streltsov and Lotko, 1996]. Observations reported by Ergun et al. [2005], however, suggest that the parallel field may not be well described by the two-fluid approach at all, and a full kinetic treatment such as those typically invoked in the study of strong double layers is required. To address the nonlinear kinetic aspects of E_{\parallel} in dispersive Alfvén waves, Singh [2002] has employed Vlasov simulations based on a model similar to that first proposed by Mishin and Forster [1995]. In this model a double layer forms where the field-aligned current in an Alfvén wave encounters a density cavity. Significantly, Singh [2002] shows that in this case transitory parallel fields as large as 100 mV/m are possible for observed parameters. Whether such results can account for the E_{\parallel} observed from FAST cannot be confirmed from the single spacecraft measurements, and we reserve a more detailed discussion to a future study based on statistical measurements.

[30] An important feature present in these observations is the existence of inertial and dissipation subranges in the observed k-spectra characteristic of turbulence. Specifically, Figure 3e shows that the inertial subrange approximately obeys a $k^{-1.7}$ characteristics of homogeneous turbulence with dissipation (where the k-spectra begin to decrease more rapidly than this scaling law) occurring for wavenumbers where $k_{\perp}\lambda_e \geq 1$. Fluid models for the production of Alfvénic turbulence in a low beta plasma have been developed by a number of workers [e.g., Chmryev et al., 1992]. Seyler [1990] demonstrated from fluid simulations how inertial Alfvén waves above the auroral may evolve nonlinearly through collisionless tearing to produce transverse electric field power spectra that tend to a universal $k^{-5/3}$ power law as we show from observations in Figure 3e. Significantly, they showed that the observed E_{\perp}/B_{\perp} spectra obeyed the expected linear result as observed [Wahlund et al., 1998; Stasiewicz et al., 2000b] and shown here in Figure 3f. In a more recent development of this model, Seyler and Wu [2001] and Wu and Seyler [2003] have investigated the linear properties of the instabilities generating the Alfvénic turbulence in the simulation and identify a current convective interchange instability as the primary cause of the cascade to smaller scales and the cause of broadband ELF observed [Seyler and Xu, 2003]. Further comparison between the predictions of these models and observations is however required to identify the process by which the observed cascade occurs.

[31] A significant result of the extreme density depletion provide by Alfvén waves in these cavities is that the electron plasma frequency is less than the electron cyclotron frequency ($\omega_{pe} < \omega_{ce}$). Consequently, the Alfvén wave accelerated electrons within these cavities may be unstable to the cyclotron maser instability and hence such cavities may be a source for auroral kilometric radiation (AKR). An Alfvén wave source for AKR has in fact been suggested previously by Olsson et al. [2004]. This may be particularly relevant for the Alfvén wave accelerated magnetosheath and or plasma sheet electrons which after reflection from the magnetic mirror form so-called “electron conics” bracketing the electron loss cone as visible in Figures 1e particularly at $\sim 0644:55$ UT. These provide a positive dJ/dv_{\perp} and a free energy source for the cyclotron

maser instability as described by *Melrose and Dulk* [1982].

[32] Finally, the observations reported here are similar to those of “lower hybrid cavities” as first reported by *Labelle et al.* [1986] from sounding rocket observations. These structures have been observed with widths transverse to the geomagnetic field of the order of 20 m and density depletions of 10s % in which waves with frequency in the vicinity of the lower hybrid frequency are found. These have been associated with ion heating [Lynch *et al.*, 1999] and a number of mechanisms have been proposed to account for the ion heating observed [Knudsen *et al.*, 2004]. The mechanism attributed for the formation of these cavities (whereby preexisting depletions focus the lower hybrid waves, enhance the wave amplitude, provide ion heating, and thereby further density cavitation) is in essence the same as that described here for the Alfvénic cavities. However, an obvious difference is that the width of the Alfvénic cavity is much larger than the gyroradii of energized ions observed within it. Consequently, the ion heating mechanisms described by *Reitzel and Morales* [1996] and *Knudsen et al.* [2004], which rely on a gyroradii larger than the width of the cavity, may be ineffectual in the Alfvénic cavity case. Observations reported by *Pincon et al.* [1997] and theoretical work by *Seyler* [1994] and *Schuck et al.* [1998] suggested that the waves observed in lower hybrid cavities are lower-hybrid eigenmodes. It is also possible that, in the Alfvénic cavity case considered here, the observed fluctuations at the largest transverse scales could be described as transverse eigenmodes. This has been previously suggested from observations by *Stasiewicz et al.* [1997] and has been shown to occur in fluid simulations [Lu *et al.*, 2003]. The largest scales in the observations we report here are comparable to the width of the cavity and the lowest frequency oscillations observed appear to be contained within it. However, because the phase velocity of the waves is much less than that of lower hybrid waves, and in fact less than the spacecraft speed, it is significantly more difficult to reliably unravel the phase structure of the wave within the cavity than for the lower hybrid case. Because of this at this stage we are unable to conclude that we are observing transverse Alfvén eigenmodes inside the cavity.

6. Conclusions

[33] In conclusion, we have observed dispersive Alfvén waves on transverse scales including the electron inertial length and energetic ion gyroradii located in deep density depressions above the auroral ionosphere. The plasma in these cavities may be depleted by more than 50% and in the most depleted cases the ambient ionospheric plasma, usually by far the dominant plasma component at the altitudes of observation, is completely absent. In these cases the cavities are populated by energized field-aligned electrons and transversely accelerated ionospheric ions and plasmas from magnetospheric sources. The field-aligned wave Poynting flux (and hence the wave group velocity) is directed downward across the density depletion while the transverse wave Poynting flux is directed inward toward the centre of the cavities observed. There is some evidence to suggest that the wave phase velocity is oppositely directed

outward from the cavity consistent with what would be expected from the refraction on the cavity walls of an initially downward propagating wave.

[34] These observations suggest a feedback scenario for plasma loss from the ionosphere facilitated by the production of dispersive Alfvén waves on transverse density gradients and the acceleration of the plasma on the gradients by these waves. This process may begin with the focusing of Alfvén wave Poynting flux into preexisting shallow density depressions in the upper ionosphere. Such depression may be produced for example by ponderomotive effects in incoming large-scale Alfvén waves [Rankin *et al.*, 1999]. The refraction and phase mixing of these focused waves on the density gradients associated with these depressions leads to the production of small-scale Alfvén waves. These small-scale waves may interact directly with the plasma and stimulate plasma outflow from these depressions through transverse ion heating. The plasma outflow from the depression leads to steeper density gradients, which leads to more rapid production of small-scale waves, which stimulate more rapid plasma outflow resulting in deeper depressions and the formation of a density cavity. This cycle accelerates with continued incoming shear Alfvén wave Poynting flux as plasma flows more rapidly out from the cavity due the increasing rate at which energy is delivered to waves on small-scales on the steepening density gradients. In this manner density cavities above the auroral ionosphere are unstable in the presence of incoming Alfvén wave Poynting flux. Eventually, through this process individual cavities may widen and merge to yield the eroded ionospheric profile shown in Figure 1 and 2 of this report.

Appendix A

[35] The configuration of the FAST fields instrument is shown in Figure A1. We use the measured electric fields given by the potential difference between spheres 5 and 8, 7 and 8, 1 and 2, and 1 and 4. This provides two orthogonal baselines for relative phase determination in the spacecraft spin plane with $x_{58-78} = 25.5$ m and $x_{12-14} = 12$ m, respectively. We now make the assumption that there is a single wave vector (\mathbf{k}_{sp}) for each wave frequency in the spacecraft frame (ω_{sp}). Under this assumption if $\phi_{58-78}(\omega_{sp})$ and $\phi_{12-14}(\omega_{sp})$ are the phase differences measured along each baseline then $\mathbf{k}_{sp}(\omega_{sp})$ projected along each baseline is given by $\mathbf{k}_{58-78}(\omega_{sp}) = \phi_{58-78}(\omega_{sp})/x_{58-78}$ and $\mathbf{k}_{12-14}(\omega_{sp}) = \phi_{12-14}(\omega_{sp})/x_{12-14}$. Since $\mathbf{k}_{58-78}(\omega_{sp}) = \mathbf{k}_{sp}(\omega_{sp}) \cdot \mathbf{x}_{58-78}/x_{58-78}$ and $\mathbf{k}_{12-14}(\omega_{sp}) = \mathbf{k}_{sp}(\omega_{sp}) \cdot \mathbf{x}_{12-14}/x_{12-14}$ then the angle between \mathbf{k}_{sp} and the \mathbf{x}_{12-14} baseline is

$$\theta_{12-14}(\omega_{sp}) = \tan^{-1} (\phi_{58-78}(\omega_{sp})/\phi_{12-14}(\omega_{sp}) \cdot \mathbf{x}_{12-14}/x_{58-78}). \quad (A1)$$

Since the baseline orientation relative to \mathbf{B}_o is known from fluxgate magnetometer measurements it is then straightforward to find the orientation of \mathbf{k}_{sp} to \mathbf{B}_o and hence \mathbf{k}_{sp} .

[36] Figure A2a shows the wavelet transform of the electric field measurements from spheres 1 and 2 over the interval from 0644:14 UT to 0644:27 UT. The black trace in this panel represents the plasma density which has been scaled to fit in this panel. Comparing the wave spectra and

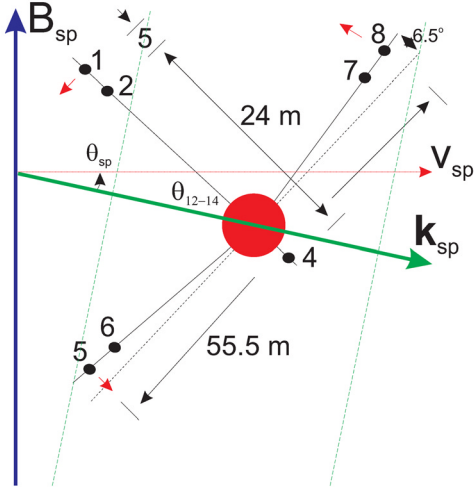


Figure A1. Electric field configuration of the FAST satellite in the spin plane.

the density measurement indicates that the wave power is enhanced in density cavities. Figure A2b shows the phase difference (ϕ_{12-14}) for the x_{12-14} baseline with the coherence for this baseline shown in Figure A2c. The same is shown for the x_{58-78} baseline in Figure A2d; however, we have omitted the coherence measurement in this case because it is almost identical to that shown in Figure A2c. The periodic variation of phase shown in Figures A2b and A2c is due to the spacecraft rotation and the relative orientation of \mathbf{k} and the dipole in the spin plane. Since $\phi_{12-14} = \mathbf{x}_{12-14} \cdot \mathbf{k}_{sp}$ and $\phi_{58-78} = \mathbf{x}_{58-78} \cdot \mathbf{k}_{sp}$ and the rest frame wave frequency is given by $\omega = \omega_{sp} - \mathbf{k}_{sp} \cdot \mathbf{v}_{sp}$, then the variation of the measured phase with spacecraft rotation is

$$\phi_{12-14} = x_{12-14}((\omega_{sp} - \omega)/(v_{sp} \cos \theta_{sp})) \cos \theta_{12-14} \quad (\text{A2})$$

and

$$\phi_{78-58} = x_{78-58}((\omega_{sp} - \omega)/(v_{sp} \cos \theta_{sp})) \cos \theta_{78-58}, \quad (\text{A3})$$

where θ_{sp} is the angle between \mathbf{k}_{sp} and the spacecraft velocity vector. Clearly, for a fixed phase, ω_{sp} is smallest when θ_{12-14} or θ_{58-78} are 0 or π and goes to infinity when θ_{12-14} or θ_{58-78} become $\pi/2$ or $3\pi/2$. This pattern is represented in Figures A2b and A2d by the U-shaped variations in phase with singularities at half the satellite spin period. At these singularities for a given ϕ , the spacecraft frame frequency $\omega_{sp} \rightarrow \infty$, indicating that \mathbf{k}_{sp} and \mathbf{x} at this spin phase are orthogonal. Comparing the form of Figure A2b with the angle between x_{12-14} and B_o in the spin plane shown in A2e suggests that \mathbf{k}_{sp} is very nearly perpendicular to the geomagnetic field and parallel/antiparallel to \mathbf{v}_{sp} .

[37] In general, Figures A2b and A2d show that with increasing frequency, in the spacecraft frame, the magnitude of the phase difference between each dipole pair increases toward $|\pi|$ radians and then decreases. This change in the sign of the slope of phase with frequency occurs where the longest electric field dipole for each baseline matches half the wavelength projected along the dipole leading to an

antenna null. The measured phase difference where this occurs is given by $\phi_{12-14} = \pm\pi(1 - x_{12}/x_{14}) = \pm 0.8\pi$ and $\phi_{58-78} = \pm\pi(1 - x_{78}/x_{58}) = \pm 0.9\pi$. Once these phase differences have been exceeded the measured phase needs to be corrected to give the actual phase as

$$\hat{\phi}_{12-14} = \phi_{12-14} \text{ if } |\phi_{12-14}| \leq 0.8\pi \quad (\text{A4})$$

$$\hat{\phi}_{12-14} = 2 \cdot \text{Sign}(\phi_{12-14})0.8\pi - \phi_{12-14} \text{ if } |\phi_{12-14}| > 0.8\pi$$

and

$$\hat{\phi}_{58-78} = \phi_{58-78} \text{ if } |\phi_{58-78}| \leq 0.9\pi \quad (\text{A5})$$

$$\hat{\phi}_{58-78} = 2 \cdot \text{Sign}(\phi_{58-78})0.9\pi - \phi_{58-78} |\phi_{58-78}| > 0.9\pi$$

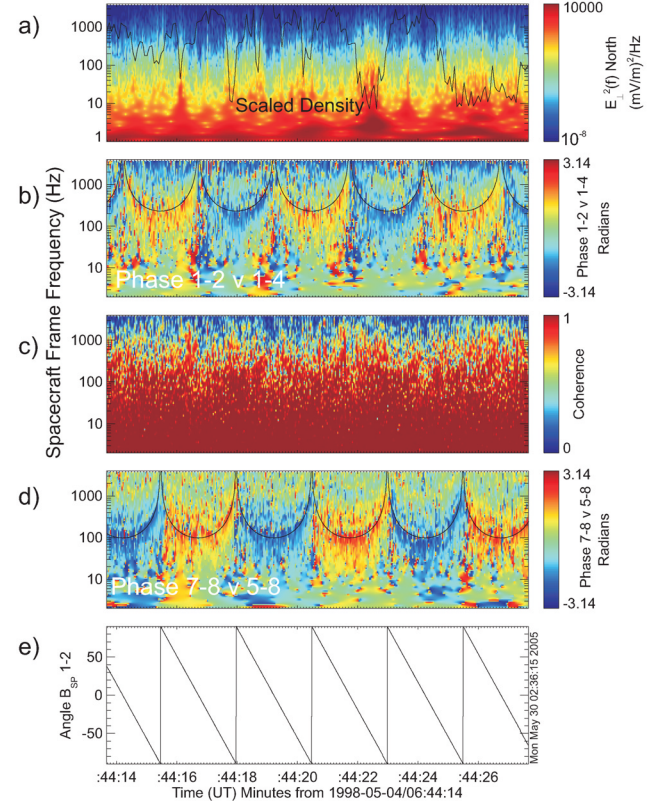


Figure A2. Phase measurements in the spin plane. (a) Wavelet spectrogram of the perpendicular to B_o northward pointing electric field (E_x or E_{\perp}). The black trace in this panel shows the density scaled to fit in this panel. (b) Relative phase between the 1–2 and 1–4 electric field dipoles. The black line in this trace is the predicted spacecraft frame frequency for Doppler shifted structures with transverse size equal to the length of the 1–4 dipole. (c) Two-point coherence of the measurements from the 1–2 and 1–4 dipoles. (d) Same as Figure A2b except for the 7–8 and 5–8 dipoles. The black line in this panel is the predicted spacecraft frame frequency for Doppler shifted structures with transverse size equal to the length of the 5–8 dipole. (e) The angle between the 1–2 dipole and the projection of the geomagnetic field (B_o) into the spin plane (B_{sp}).

Further nulls can be expected as the wavelengths approach the dimensions of the other electric field dipoles; however, these are beyond the frequency range where high coherence is obtained and do not effect the results reported here.

[38] If we momentarily assume that the transverse phase velocity of the observed fluctuations is much less than the spacecraft speed (i.e., that the observed phase structuring is due largely to Doppler shift), then $\omega \approx k_{sp} \cdot v_{sp}$ and we can predict the variation of the phase nulls with frequency in the spacecraft frame [Temerin, 1979]. From previously we found that roughly $k_{sp} \parallel v_{sp}$. In this case equation (2) and equation (3) can be rearranged to give the variation of spacecraft frame frequency with phase as

$$f_{12-14} = v_{sp} \left/ \left(\frac{\phi_{12-14}}{2\pi} \cdot x_{12-14} \cos \theta_{12-14} \right) \right. \quad (\text{A6})$$

and

$$f_{78-58} = v_{sp} \left/ \left(\frac{\phi_{78-58}}{2\pi} \cdot x_{78-58} \cos \theta_{78-58} \right) \right. \quad (\text{A7})$$

Substituting the angle for the nulls into these expressions gives the curves shown in Figures A2b and A2d. The close agreement with the variation of the frequency and phase shown by these curves and the frequency of the observed nulls indicates that the assumptions of transverse wave phase speeds less than the spacecraft speed and of k_{sp} largely perpendicular to \mathbf{B}_o (and so also parallel/antiparallel to v_{sp}) are reasonable. This can be used as a simple check on the more complete analysis using equation (A1) where these assumptions are removed as implemented in section 3.

[39] **Acknowledgments.** This research was supported by NASA grants NAG-12784, NAG-12954, NAG-12453, and NAG3-3596. Chris Chaston is indebted to Ming Chung Chu and the Physics Department at the Chinese University of Hong Kong where much of this work was completed and to Vincent Genot and the CESR Toulouse France.

[40] Arthur Richmond thanks Robert Rankin and Charles E. Seyler for their assistance in evaluating this paper.

References

- Andersson, L., N. Ivchenko, J. Clemons, A. A. Namgaladze, B. Gustavsson, J. E. Wahlund, L. Eliasson, and R. Y. Yurik (2002), Electron signatures and Alfvén waves, *J. Geophys. Res.*, **107**(A9), 1244, doi:10.1029/2001JA000096.
- Bellan, P., and K. Stasiewicz (1998), Fine scale cavitation of ionospheric plasma caused by inertial Alfvén wave ponderomotive force, *Phys. Rev. Lett.*, **80**, 3523.
- Chaston, C. C., C. W. Carlson, W. J. Peria, R. E. Ergun, and J. P. McFadden (1999), FAST observations of inertial Alfvén waves in the dayside aurora, *Geophys. Res. Lett.*, **26**, 647.
- Chaston, C. C., C. W. Carlson, R. E. Ergun, and J. P. McFadden (2000), Alfvén waves, density cavities and electron acceleration observed from the FAST spacecraft, *Phys. Scr. T*, **84**, 64.
- Chaston, C. C., J. B. Bonnell, C. W. Carlson, J. P. McFadden, R. E. Ergun, and E. J. Lund (2004), Ion acceleration in dispersive Alfvén waves, *J. Geophys. Res.*, **109**, A04205, doi:10.1029/2003JA010053.
- Chaston, C. C., T. D. Phan, J. W. Bonnell, F. S. Mozer, M. Acuna, M. L. Goldstein, A. Balogh, M. Andre, H. Reme, and A. Fazakerley (2005), Drift-kinetic Alfvén waves observed near a reconnection X line in the Earth's magnetopause, *Phys. Rev. Lett.*, **95**, 065002.
- Chen, L., Z. Lin, and R. White (2001), On resonant heating below the cyclotron frequency, *Phys. Plasmas*, **8**, 4713.
- Chmyrev, V. M., V. A. Marchenko, O. A. Pokhotelov, P. K. Shukla, L. Stenflo, and A. V. Strelets (1992), The development of discrete active auroral forms, *IEEE Trans. Plasma Sci.*, **20**, 764.
- Chust, T., P. Louarn, M. Volwerk, H. De Feraudy, A. Roux, J.-E. Wahlund, and B. Holback (1998), Electric fields with a large parallel component observed by Freja spacecraft: Artifacts or real signals?, *J. Geophys. Res.*, **103**, 215.
- Ergun, R. E., L. Andersson, Y.-J. Su, D. L. Newman, M. V. Goldman, W. Lotko, C. C. Chaston, and C. W. Carlson (2005), Localized parallel electric fields associated with inertial Alfvén waves, *Phys. Plasmas*, **12**, 072901.
- Genot, V., P. Louarn, and D. Le Queau (1999), A study of the propagation of Alfvén waves in auroral density cavities, *J. Geophys. Res.*, **104**, 22,649.
- Genot, V., P. Louarn, and F. Mottez (2000), Electron acceleration by Alfvén waves in density cavities, *J. Geophys. Res.*, **105**, 27,611.
- Genot, V., P. Louarn, and F. Mottez (2001), Fast evolving spatial structure of auroral parallel electric fields, *J. Geophys. Res.*, **106**, 29,633.
- Genot, V., P. Louarn, and F. Mottez (2004), Alfvén wave interaction with homogeneous plasmas: Acceleration and energy cascade toward smaller scales, *Ann. Geophys.*, in press.
- Goertz, C. K., and R. W. Boswell (1979), Magnetosphere-ionosphere coupling, *J. Geophys. Res.*, **84**, 7239.
- Hasegawa, A. (1976), Particle acceleration by MHD surface wave and formation of aurora, *J. Geophys. Res.*, **81**, 5083.
- Johnstone, A. D., and J. D. Winningham (1982), Satellite observations of suprathermal electron bursts, *J. Geophys. Res.*, **87**, 2321.
- Kletzing, C. A. (1994), Electron acceleration by kinetic Alfvén waves, *J. Geophys. Res.*, **99**, 11,095.
- Knudsen, D. J., and J.-E. Wahlund (1998), Core ion flux bursts within solitary kinetic Alfvén waves, *J. Geophys. Res.*, **103**, 4157.
- Knudsen, D. J., et al. (2004), Lower Hybrid cavity density depletions as a result of transverse ion acceleration localized on the gyro-radius scale, *J. Geophys. Res.*, **109**, A04212, doi:10.1029/2003JA010089.
- Labelle, J., and P. M. Kintner (1989), The measurement of wavelength in space plasmas, *Rev. Geophys.*, **27**, 495.
- Labelle, J., P. Kintner, A. W. Yau, and B. A. Whalen (1986), Large amplitude wave packets observed in the ionosphere in associations with transverse ion acceleration, *J. Geophys. Res.*, **91**, 7113.
- Li, X., and M. Temerin (1993), Ponderomotive effects on ion acceleration in the auroral zone, *Geophys. Res. Lett.*, **20**, 13.
- Louarn, P., J.-E. Wahlund, T. Chust, H. de Feraudy, A. Roux, B. Holback, P.-O. Dovner, A. I. Eriksson, and G. Holmgren (1994), Observations of kinetic Alfvén waves by the Freja satellite, *Geophys. Res. Lett.*, **21**, 1847.
- Lu, J. Y., R. Rankin, R. Marchand, and V. T. Tikhonchuk (2003), Nonlinear acceleration of dispersive effects in field line resonances, *Geophys. Res. Lett.*, **30**(10), 1540, doi:10.1029/2003GL016929.
- Lynch, K. A., R. L. Arnoldy, P. M. Kintner, P. Schuck, J. W. Bonnell, and V. Coffey (1999), Auroral ion acceleration from lower hybrid solitary structures: A summary of sounding rocket observations, *J. Geophys. Res.*, **104**, 28,515.
- Lysak, R. L. (1998), The relationship between electrostatic shocks and kinetic Alfvén waves, *Geophys. Res. Lett.*, **25**, 2089.
- Lysak, R. L., and C. W. Carlson (1981), Effect of microturbulence on magnetosphere-ionosphere coupling, *Geophys. Res. Lett.*, **8**, 269.
- Lysak, R. L., and C. T. Dum (1983), Dynamics of magnetosphere-ionosphere coupling including turbulent transport, *J. Geophys. Res.*, **88**, 365.
- Maggs, J. E., and G. J. Morales (1996), Magnetic fluctuations associated with field-aligned striations, *Geophys. Res. Lett.*, **23**, 633.
- Melrose, D. B., and G. A. Dulk (1982), Electron-cyclotron masers as the source of certain solar and stellar radio bursts, *Astrophys. J.*, **259**, 844.
- Mishin, E. V., and M. Forster (1995), Alfvénic shocks and low altitude auroral acceleration, *Geophys. Res. Lett.*, **22**, 1745.
- Mottez, F., J. C. Adams, and A. Heron (1998), A new guiding center PIC scheme for electromagnetic highly magnetized plasma simulation, *Comput. Phys. Commun.*, **113**, 1.
- Mozer, F. S., C. W. Carlson, M. K. Hudson, R. B. Torbert, B. Parady, J. Yattee, and M. C. Kelley (1977), Observations of paired electrostatic shocks in the polar magnetosphere, *Phys. Rev. Lett.*, **38**, 292.
- Olsson, A., P. Janhunnen, J. Hasnatz, M. Mogilevsky, S. Perraut, and J. D. Menietti (2004), Observational study of generation conditions of sub-storm associated low-frequency AKR emissions, *Ann. Geophys.*, **22**, 3571.
- Pincon, J. L., P. M. Kintner, P. W. Schuck, and C. E. Seyler (1997), Observation and analysis of lower hybrid solitary structures as rotating eigenmodes, *J. Geophys. Res.*, **102**, 17,283.
- Rankin, R., J. C. Samson, V. T. Tikhonchuk, and I. Voronkov (1999), Auroral density fluctuations on dispersive field line resonances, *J. Geophys. Res.*, **104**, 4399.
- Rankin, R., R. Marchand, J. Y. Lu, K. Kabin, and V. T. Tikhonchuk (2005), Theory of dispersive shear Alfvén wave focusing in Earth's magnetosphere, *Geophys. Res. Lett.*, **32**, L05102, doi:10.1029/2004GL021831.

- Reitzel, K. J., and G. J. Morales (1996), Perpendicular ion acceleration in field-aligned density striations, *J. Geophys. Res.*, **101**, 27,177.
- Ronnmark, K. (1999), Electron acceleration in the auroral current circuit, *Geophys. Res. Lett.*, **26**, 983.
- Seyler, C. E. (1990), A mathematical model of the structure and evolution of small-scale discrete auroral arcs, *J. Geophys. Res.*, **95**, 17,199.
- Seyler, C. E. (1994), Lower hybrid wave phenomena associated with density depletions, *J. Geophys. Res.*, **99**, 19,513.
- Seyler, C. E., and K. Wu (2001), Instability at the electron inertial scale, *J. Geophys. Res.*, **106**, 21,623.
- Seyler, C. E., and T. Xu (2003), The relationship between field-aligned currents and low frequency electromagnetic fluctuations, *Geophys. Res. Lett.*, **30**(21), 2106, doi:10.1029/2003GL018292.
- Seyler, C. E., J.-E. Wahlund, and B. Holback (1995), Theory and simulation of low frequency plasma waves and comparison to Freja satellite observations, *J. Geophys. Res.*, **100**, 21,453.
- Schuck, P. M., C. E. Seyler, J.-L. Pinçon, J. W. Bonnell, and P. M. Kintner (1998), Theory, simulation and observation of discrete eigenmodes associated with lower hybrid solitary structures, *J. Geophys. Res.*, **103**, 6935.
- Shuck, P. W., J. W. Bonnell, and P. M. Kintner (2003), A review of lower hybrid solitary structures, *IEEE Trans. Plasma Sci.*, **31**, 1125.
- Shukla, P., and L. Stenflo (1999), Plasma density cavitation due to inertial Alfvén wave heating, *Phys. Plasmas*, **6**, 4120.
- Singh, N. (2002), Spontaneous formation of current-driven double layers in density depletions and its relevance to solitary Alfvén waves, *Geophys. Res. Lett.*, **29**(7), 1147, doi:10.1029/2001GL014033.
- Sugiura, M. (1984), A fundamental magnetosphere-ionosphere mode involving field-aligned currents as deduced from DE-2 observations, *Geophys. Res. Lett.*, **11**, 877.
- Stasiewicz, K., G. Gustaffson, G. Marklund, P.-A. Lindqvist, J. Clemons, and L. Zanetti (1997), Cavity resonators and Alfvén resonance cones observed on Freja, *J. Geophys. Res.*, **102**, 2565.
- Stasiewicz, K., G. Holmgren, and L. Zanetti (1998), Density depletions and current singularities observed by Freja, *J. Geophys. Res.*, **103**, 4251.
- Stasiewicz, K., et al. (2000a), Small scale Alfvénic structure in the aurora, *Space Sci. Rev.*, **92**, 423.
- Stasiewicz, K., Y. Khotyaintsev, M. Berthomier, and J.-E. Wahlund (2000b), Identification of widespread turbulence of dispersive Alfvén waves, *Geophys. Res. Lett.*, **27**, 173.
- Stasiewicz, K., et al. (2000c), Stochastic ion heating by orbit chaotization on electrostatic waves and non-linear structures, *Phys. Scr. T*, **84**, 60.
- Streltsov, A., and W. Lotko (1996), The fine structure of dispersive, non-radiative field line resonances, *J. Geophys. Res.*, **100**, 5343.
- Su, Y.-J., S. T. Jones, R. E. Ergun, and S. E. Parker (2004), Modelling of field-aligned electron bursts by dispersive Alfvén waves in the day-side auroral region, *J. Geophys. Res.*, **109**, A11201, doi:10.1029/2003JA010344.
- Temerin, M. (1979), Doppler shift effects on double-probe measured electric field power spectra, *J. Geophys. Res.*, **84**, 5929.
- Thompson, B. J., and R. L. Lysak (1996), Electron acceleration by inertial Alfvén waves, *J. Geophys. Res.*, **101**, 5359.
- Wahlund, J.-E., P. Louarn, T. Chust, H. de Feraudy, A. Roux, B. Holback, P.-O. Dovner, and G. Holmgren (1994), On ion acoustic turbulence and nonlinear evolution of kinetic Alfvén waves in aurora, *Geophys. Res. Lett.*, **21**, 1831.
- Wahlund, J.-E., et al. (1998), Broadband ELF plasma emission during energization: 1. Slow ion acoustic waves, *J. Geophys. Res.*, **103**, 4343.
- Wu, K., and C. E. Seyler (2003), Instability of inertial Alfvén waves in transverse sheared flows, *J. Geophys. Res.*, **108**(A6), 1236, doi:10.1029/2002JA009631.

J. W. Bonnell, C. W. Carlson, C. C. Chaston, and J. P. McFadden, Space Sciences Laboratory, University of California, Berkeley, Centennial Drive at Grizzly Peak Blvd, Berkeley, CA 94720-7450, USA. (ccc@ssl.berkeley.edu)

R. E. Ergun, Laboratory for Atmospheric and Space Physics, University of Colorado, 1234 Innovation Drive Campus Box, Boulder, CO 80303–0000, USA.

V. Genot, Centre d'Etude Spatiale Rayonnements, 9 Av. Colonel Roche, F-31400, Toulouse, France.

K. J. Hwang, Physics and Astronomy, Dartmouth College, 6127 Wilder Lab, Hanover, NH 03755-0000, USA.

E. J. Lund, Space Science Center, University of New Hampshire, Morse Hall, 39 College Road, Durham, NH 03824, USA.

R. J. Strangeway, Institute for Geophysical and Planetary Physics, University of California, Los Angeles, 2712 Geology Bldg., 405 Hilgard Ave., Los Angeles, CA 90095, USA.